Nuclear Science and Techniques (2025) 36:217
https://doi.org/10.1007/s41365-025-01797-y

Development and characteristics of a superconducting resonator and cryogenic low-noise amplifiers for Shanghai Penning Trap

Jia-Rong Wang[1,2] · Ji-Fei Wu[1,2] · Tian-Hang Zhang[1,2] · Jia-Lin Liu[1] · Jia-Teng Peng[3] · Jia-Wei Wang[2,3] · Yang Shen[1,2] · Bao-Ren Wei[1,2] · Ya-Ming Zou[1,2] · Bing-Sheng Tu[1,2]

Received: 23 July 2024 / Revised: 17 February 2025 / Accepted: 22 February 2025 / Published online: 31 August 2025

Abstract

Accurate atomic mass data hold significant application value in various research fields, in which Penning trap mass spectrometry is considered the most precise experimental method. A cryogenic detection system is a key component for reading out the image charge of charged particles in Penning traps using the Fourier transform ion cyclotron resonance technique. In this paper, we present the development and characteristics of this detection system, which includes a superconducting resonator and cryogenic low-noise amplifiers. The resonator consists of delicately woven thin NbTi wires configured into a multilayer helical coil, offering a quality factor of 98004 at around 1 MHz. Low-noise amplifiers are developed based on GaAs field effect transistors, exhibiting amplification factors greater than 27 dB with a power consumption of approximately 6 mW in the frequency range of 0.1 to 10 MHz. The lowest input voltage noise is 0.8 nV/$\sqrt{\text{Hz}}$ at 1 MHz. The fabrication process, operation, and measurements are elucidated in detail.

Keywords Penning traps · Image charge detection · Cryogenic electronics

1 Introduction

The mass of an atom, a fundamental property that inherently connects the atomic and nuclear binding energies, is a unique fingerprint of the atomic nucleus, providing hints on atomic and nuclear structures, as well as the interactions between fundamental particles such as electrons and nuclei, protons, and neutrons [1, 2]. Accurate atomic mass data have significant application value in various physics research fields, including nuclear models, nuclear astrophysics, weak interaction studies, and metrology [1, 3, 4]. In addition, by observing minute deviations from the theory, potential new interactions beyond the standard model (SM) can be probed [5, 6].

Numerous studies have been performed to precisely measure atomic masses using different techniques of mass spectrometry [2]; for example, isochronous mass spectrometry (IMS) [7–10] and Schottky mass spectrometry (SMS) [11, 12] at storage rings, time-of-flight magnetic-rigidity (TOF-Bρ) method [13], multireflection TOF mass spectrometry (MR-TOF-MS) [14], and Penning trap mass spectrometry [15]. Mass spectrometry based on storage rings is a suitable method for the mass measurement of radioactive beams [16–20]. Recently, the CSRe/IMP group installed a double time-of-flight detector system to improve the measurement accuracy to below 10^{-6} [18, 21, 22] and precisely determined the masses of a few neutron-deficient nuclei [23–26] for nuclear structure and astrophysics interest. The

This work was supported by the National Key R&D Program of China (No. 2023YFA1606501), the National Natural Science Foundation of China (Nos. 12204110 and 12474251), Shanghai Pujiang Program (No. 22PJ1401100), Max-Planck Partner Group Project, and the Fudan University Yan Liyuan - EnSiKai Foundation (JX240003).

✉ Yang Shen
shenyang@fudan.edu.cn

✉ Bing-Sheng Tu
bingshengtu@fudan.edu.cn

[1] Institute of Modern Physics, Fudan University, Shanghai 200433, China

[2] Key Laboratory of Nuclear Physics and Ion-Beam Application (MOE), Fudan University, Shanghai 200433, China

[3] Department of Nuclear Science and Technology, Fudan University, Shanghai 200433, China

MR-ToF method was implemented at the GSI [27] RIKEN [28] and TITAN [29] aim to measure short-lived nuclei with resolution powers greater thatn 10^5 and flight times shorter than a few milliseconds.

Penning trap mass spectrometry is considered the most precise measurement method for atomic mass owing to its extremely high accuracy at 10^{-9} or below. Using a novel phase-imaging ion cyclotron resonance (PI-ICR) technique developed by Eliseev et al. [30], the SHIPTRAP group reported the precise measurement of superheavy element masses [31]. Similar techniques have also been implemented in other online Penning trap facilities, such as JYFLTRAP [32] and TITAN [33] for the measurement of short-lived nuclei. For long-lived or stable species, the precision achievable by Penning trap mass spectrometry is even higher, up to 10^{-11}, using the Fourier transform ion cyclotron resonance (FT-ICR) technique. The higher accuracy is simply due to the longer measurement times required for stable nuclei, because the measurement precision is inversely proportional to the observation time $1/T_{\mathrm{obs}}$. FT-ICR penning trap mass spectrometry is the most powerful tool for the experimental determination of atomic masses, such as electrons [34], protons [35] and even antimatters [36], providing the most accurate measurement of fundamental parameters and a stringent test of the building blocks of the SM.

FT-ICR is a nondestructive measurement technique capable of detecting single ions in Penning traps. The ions oscillating in the electromagnetic field can induce image currents in the trap electrodes, which are typically a few fA and have frequency features identical to the eigenmotions of the ions. In 1992, Jefferts et al. [37] described the development of a detection system consisting of a superconducting inductor and a GaAs field effect transistor preamplifier for image current signal readout. Subsequently, Ulmer et al. [38] presented an optimization procedure for a helical superconducting resonator, whereas Nagahama et al. [39] reported another design for a toroidal resonator with extremely high quality factors. Currently, this detection system is indispensable for precision Penning trap mass spectrometry based on the FT-ICR method [40].

A new cryogenic Penning trap setup is currently under construction in Shanghai, China. The goal of this Penning trap is to detect the decay of long-lived electronic metastable states in a single ion confined within the trap directly, such as $3s^2 3p^5 3d\ ^3F_4$ of $^{56}Fe^{8+}$ with a life time of 1110 s [41], which requires extremely high mass accuracy at 10^{-11} or even above. To this end, a cryogenic detection system for reading out the image charges of trapped ions must be developed. In this study, the original design described in Ref. [40], helical superconducting resonators, and low-noise high-gain cryogenic amplifiers. This article introduces the fundamental principle of Penning traps and the nondestructive image charge detection technique (Sect. 2). Then, we present the design of the cryogenic radio-frequency (RF) amplifiers and superconducting resonator as well as experimental tests on their performance at a cold-head base cryogenic stage (Sect. 3). Finally, we summarized the characteristics of the proposed detection system and predicted its potential improvements.

2 Principle of penning trap

2.1 Ion motion in a penning trap

In a homogeneous magnetic field, a charged particle with mass m and charge q experiences a Lorentz force $\vec{F} = q\vec{v} \times \vec{B}$, and subsequent circular motion with free-space cyclotron frequency:

$$\nu_{\mathrm{c}} = \frac{1}{2\pi}\frac{qB}{m}, \tag{1}$$

where ν_{c} is the frequency of ion motion in a pure magnetic field. To confine the ions in all spatial directions, a quadruple electrostatic potential was superimposed along the axial axis. The quadrupolar electric potential $U(r, z)$ takes the following form:

$$U(r,z) = \frac{U_0}{2d^2}\left(z^2 - \frac{r^2}{2}\right), \tag{2}$$

where U_0 is the potential difference between the end cap and ring electrodes, d is the characteristic dimension of the Penning trap. The potential can be generated by employing two electrodes shaped as infinite revolution hyperboloids. In practice, a semi-quadratic electric potential in the central region is primarily generated using two geometries: (a) two finite hyperboloids of revolution with two additional correction electrodes and (b) a stack of several (typically five) cylindrical electrodes or other exotic geometries [42]. The fields were oriented such that an electrostatic potential well was created along the magnetic field lines. In this configuration, the magnetic field confines ion motion to the plane perpendicular to the magnetic field lines (radial motion), whereas the electrostatic potential traps ions along the magnetic field lines (axial motion). A detailed theory of the Penning trap can be found elsewhere [43].

The presence of an electrostatic quadrupolar field modifies the pure cyclotron motion of an ion in the magnetic field, resulting in three independent eigenmotions with frequencies

$$\nu_+ = \frac{\nu_{\mathrm{c}}}{2} + \sqrt{\frac{{\nu_{\mathrm{c}}}^2}{4} - \frac{{\nu_z}^2}{2}}, \tag{3}$$

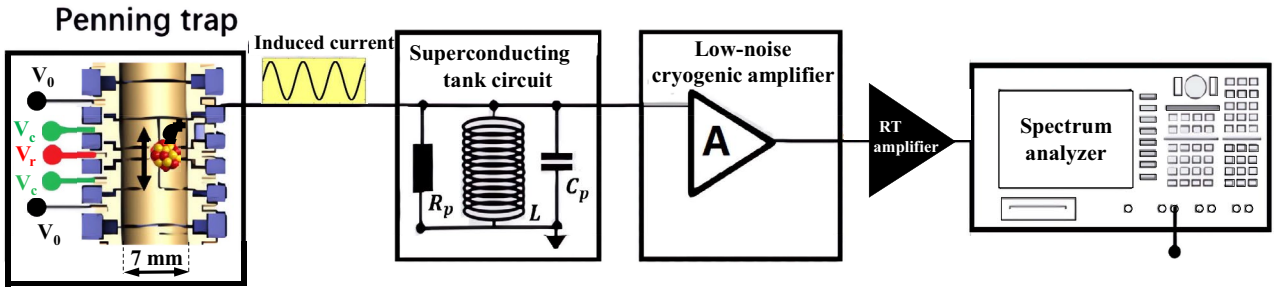

Fig. 1 (Color online) Schematic of image charge detection system in a cryogenic Penning trap, which consists of a LC tank circuit and a low-noise cryogenic amplifier. The cut model shows a typical five-electrode (gold) penning trap with sapphire insulation spacers (blue). The endcap electrodes V_0 (black) are connected to ground and the ring electrode V_r (red) as well as the correction electrodes V_c (green) are supplied by negative voltages. The oscillation of the charged particle in the axial direction is indicated by the double-headed arrow. The resonator can be represented as an inductance L, an effective resistance R_p and a parasitic capacitance C_p. The signal through the resonator is then coupled to a low-noise cryogenic amplifier before entering a room-temperature (RT) amplifier and a spectrum analyzer

$$\nu_- = \frac{\nu_c}{2} - \sqrt{\frac{\nu_c^2}{4} - \frac{\nu_z^2}{2}}, \tag{4}$$

$$\nu_z = \frac{1}{2\pi}\sqrt{\frac{qU_0}{md^2}}, \tag{5}$$

where ν_+, ν_- and ν_z are the frequencies of the Modified cyclotron, magnetron, and axial motions Typically, ν_+ is over ten MHz, ν_z is several hundreds of kilohertz, and ν_- is of the order of kilohertz according to the Shanghai Penning Trap design [41]. The free cyclotron frequency can be determined from the invariance theorem ${\nu_c}^2 = {\nu_+}^2 + {\nu_-}^2 + {\nu_z}^2$ [44], which links the eigenfrequencies to the charge to mass ratio of an ion. This relation is applicable not only to an ideal Penning trap but also to existing Penning trap systems with small imperfections in the alignment of the electric and magnetic fields.

2.2 Principle of image charge detection

The frequency of motion of a single ion is determined through the utilization of the FT-ICR technique. The detection principle is illustrated in Fig. 1. The oscillating charged particles induce an image current in the trap electrodes. With a large impedance, this small current signal is converted into a detectable voltage. This impedance is realized by a superconducting inductor L connected in parallel to the trap, forming a tank circuit with parasitic capacitance C_p and a resonance frequency ν_{res}

$$\nu_{res} = \frac{1}{2\pi}\sqrt{\frac{1}{LC_p}}. \tag{6}$$

The serial ohmic and dielectric losses were converted into large parallel resistances. Once the ion oscillates in resonance with the tank circuit, the resonator acts as a pure resistor R_p:

$$R_p = 2\pi\nu_{res}QL, \tag{7}$$

where Q is the circuit-quality factor. In this case, the ions can be cooled using a resonator. Once the particle reaches thermal equilibrium with the resonator at the cryogenic temperature (typically at the liquid-helium temperature), its motional energy dissipates into the tank circuit, producing an image current typically on the order of a few fA. Thus, a cryogenic detection system with a high Q value and low input noise is essential for signal amplification prior to the Fourier transformation in a spectrum analyzer at RT.

3 Cryogenic electronic detection system development

3.1 Cryogenic amplifiers

The detection system comprises two crucial components: a high-Q resonator and cryogenic low-noise amplifier. The ion signal from the trap can be affected by noise as it travels through the transmission line, which is several meters long. Therefore, using a low-noise amplifier positioned in the cryogenic region, close to the downstream of the resonator, is essential for signal amplification. Currently, most commercial amplifiers with a bandwidth that meets the ion frequencies in Penning traps cannot operate at liquid-helium temperatures because the charge carriers in standard silicon semiconductors can freeze. In addition, some amplifiers suffer from high power consumption and significant input noise, rendering them unsuitable for very weak image charge signals. A desirable amplifier requires low noise and power

consumption, along with a suitable bandwidth in the range of a few hundred kHz to tens of MHz.

The first low-noise cryogenic amplifier design, denoted AMP1 is shown in Fig. 2, where the core component, a GaAs-based field effect transistor (MESFET), was tested with excellent performance at cryogenic temperatures. In this design, the first stage comprised a cascode common-source amplifier with two FETs to mitigate the Miller effect. This significantly reduces the amplifier's back-action on the resonator's quality factor caused by the parasitic Miller capacitance. The second stage is a standard common-source amplifier connected to the output of the first stage for additional amplification. The third stage, which is also called a source follower, does not amplify the signal but rather aims for impedance matching. The entire fabrication process utilized a printed circuit board (PCB) technique, with a polytetrafluoroethylene (PTFE) substrate to minimize dielectric loss. All electronic components, including FETs denoted here as Q1 to Q4, resistors, and capacitors, are surface-mountable, resulting in an amplifier board with dimensions 20 mm × 40 mm and 1.5 mm in thickness. We used metal film resistors and stacked metallized film chip capacitors with a low-temperature drift. Note that all the FETs used in this study were dual-gate GaAs transistors. However, we shortened the two gates Q1 and Q2 in the cascode stage to increase the channel length and thus reduce the 1/*f*-noise of the transistor in the low-frequency range. Another FET, referred to as Q5, was placed on the PCB board (not shown in the design sheet). The dual-gate FET aims to replace the cascode stage for comparison. The signal input and output were coupled via SMA connectors. The four FETs on the PCB board were operated with a total of six bias voltages, denoted here as Vg1, Vg2, and Vd1 for cascode stage gates and drain voltages, Vg3 and Vd1 for the second-stage gate and drain voltages, and Vg4 and Vd2 for the source-follower gate and drain voltages. In practice, Vg1 and Vg3 control the opening of the first and second stages, respectively, whereas Vg2 and Vg4 are grounded to reduce the number of voltage supply channels. The first and second stages share the same drain voltage, whereas a separate drain voltage supplied to the third stage can reduce power consumption. Consequently, the resulting total power consumption of the amplifier was approximately 6 m watts .

The gain and noise features of the amplifier are mainly determined by the FETs, and the first transistor (Q1) among the four FETs on the PCB board has the most significant impact on the input noise. In this study, we evaluate the performance of a low-noise amplifier using various FETs placed at Q1. The measurements were performed at the cold-head base 4 K cryogenic stage. A transmission network was established to measure the amplifier gain, as shown in Fig. 3a. A vector network analyzer was used to deliver and receive the RF signal. The input voltage noise of the amplifier was measured using a spectrum analyzer, which included an additional RT amplifier with a known gain in the network, as shown in Fig. 3b. The cryogenic amplifier input is then grounded. The noise spectrum measured by the spectrum analyzer has the following form:

$$N_{\mathrm{meas}} = \sqrt{(N_{\mathrm{cryo}}^2 \cdot G_{\mathrm{cryo}}^2 + N_{\mathrm{RT}}^2) \cdot G_{\mathrm{RT}}^2 + N_{\mathrm{SpA}}^2}, \tag{8}$$

where N_{cryo}, N_{RT} and N_{SpA} represent the actual input voltage noise of the cryogenic amplifier, the RT amplifier and spectrum analyzer, respectively. N_{meas}, N_{RT} and N_{SpA} can be determined independently. Therefore, N_{cryo} can be calculated using the measured gains of the cryogenic amplifier G_{cryo} and RT amplifier G_{RT}.

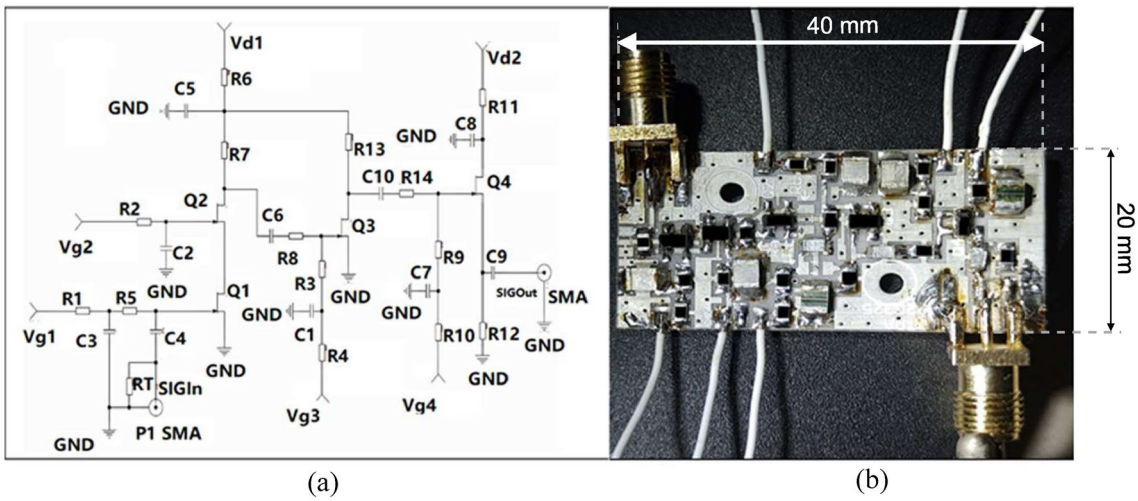

Fig. 2 (Color online) **a** Design of the low-noise cryogenic amplifier. **b** Photograph of the cryogenic amplifier, and its length and width are 20 mm and 40 mm, respectively

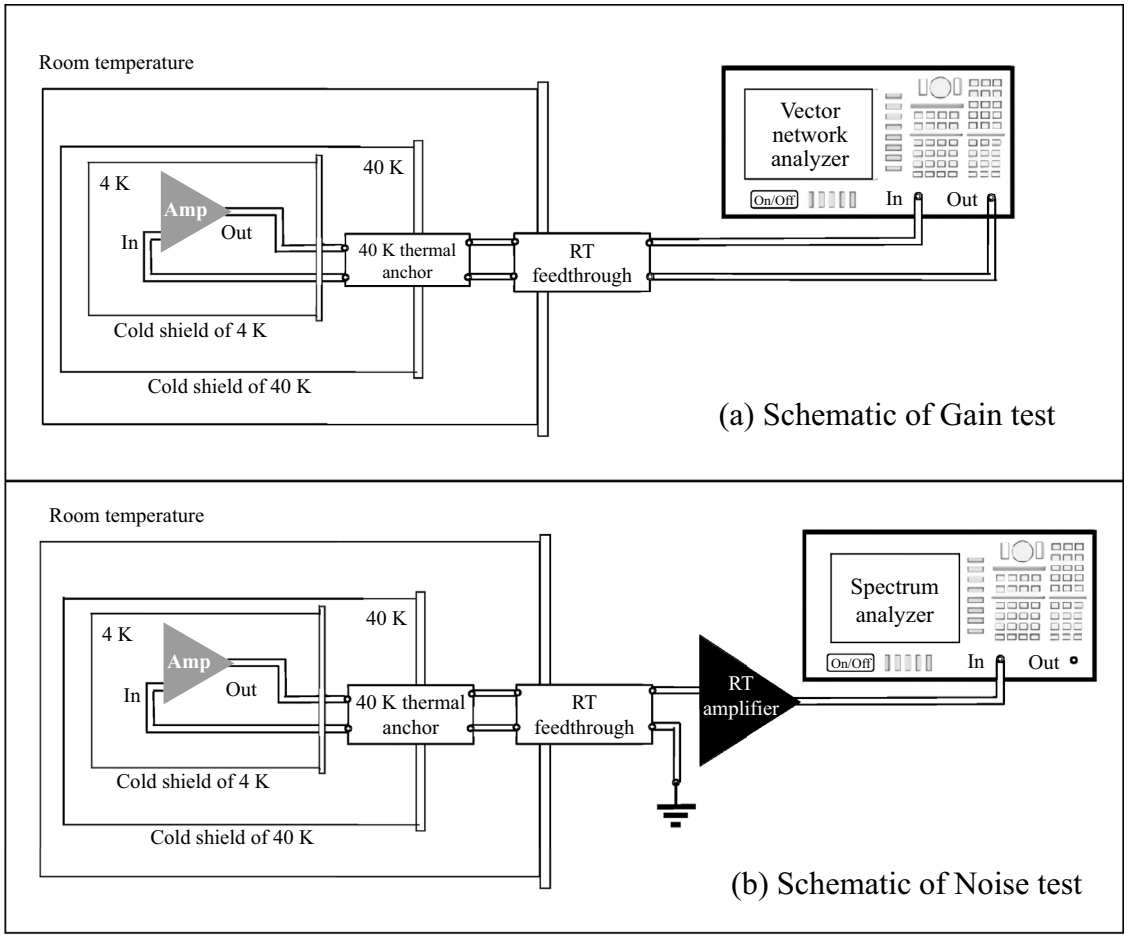

Fig. 3 Schematic of the measurement setup for the low-noise amplifier test at cryogenic stage. **a** The amplification factor (gain) of the amplifier is measured with a vector network analyzer. **b** By grounding the input of the cryogenic amplifier, the input voltage noise of the amplifier can be measured using an RT amplifier and a spectrum analyzer. For more details, see the main text

The measured forward transmission S21 and input voltage noise of the cryogenic amplifier with different first FETs at Q1 are shown in Figs. 4 and 5, respectively. The remaining components remain unchanged. Q2, Q3 and Q4 are CF739, Ne25139-U71 and CF739, respectively. For each FET, the gate voltage of each FET is tuned to the working point. In general, the amplifier with Ne25139 series at Q1 exhibited a higher amplification factor than those with 3sk164 and 3sk166 in the frequency range of 0.1 10 MHz. The input voltage noise of the amplifier, which consists of 1/*f* noise and white noise, is dominant by the noise of Q1. To detect the axial frequency of the ion in the Penning trap, input noise within the frequency range of a few hundred kilohertz to 1 MHz is critical. The voltage noise densities of the FETs are summarized in Table 1. Ne25139-U71 demonstrates the lowest 1/*f* noise, whereas the noise levels of Ne25139-U73 and 3sk166 are the highest. Notably, the measured input noise could contain noise from the transmission line because we ground the input of the amplifier at RT feedthrough.

Table 1 The voltage noise density at 1 MHz for AMP1 using different FETs at Q1 with the cascode design and CF739 at Q2

FET(Q1)	Noise ($nV/\sqrt{Hz}$)	Idss (mA)
Ne25139-U71	0.8	5–15
Ne25139-U72	1.8	10–25
Ne25139-U73	4.8	20–35
3sk164	1.5	10–35
3sk166	3.7	20–80
Ne25139-U71 wo. cas. (Q5)	1.9	5–15

Ne25139-U71 wo. cas. stands for using duel gate connection with a single Ne25139-U71 instead of the cascode design. The saturated drain-source currents (Idss) of the FETs obtained from the manual are listed

However, we did not observe any significant effect on the voltage noise density measurement.

At a sufficiently low temperature, the fluctuation of the carrier mobility owing to the random scattering of impurities

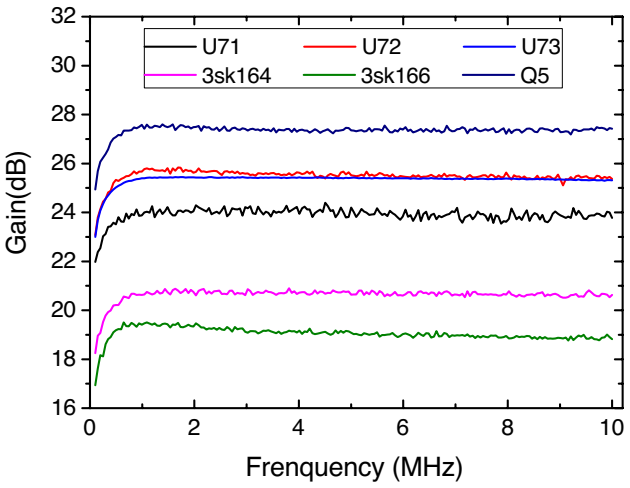

Fig. 4 (Color online) The measured gain of the AMP1 using different FETs at Q1 in the frequency range of 0.1 to 10 MHz. The gate voltages of the FETs are set to their working points. The amount of curve fluctuation is attributed to different averaging times

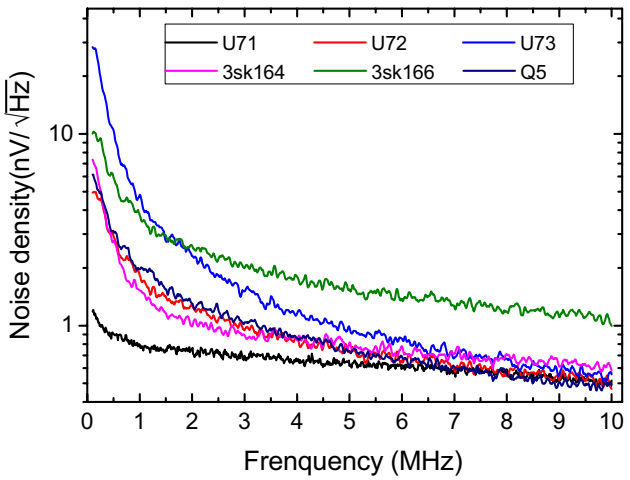

Fig. 5 (Color online) The measured voltage noise density of the AMP1 using different FETs at Q1 in the frequency range of 0.1 to 10 MHz

dominates the 1/*f* noise. This process can be described using the empirical Hooge equation

$$u_n^2 = \alpha_L \frac{I_{ds}^2 r_{ds}^2}{N L_{ch}}, \tag{9}$$

where u_n is the 1/*f* noise density, α_L is an empirical parameter dependent on the fabrication process, I_{ds} is the drain-source current, r_{ds} the effective drain-source resistance, N the number of free charges in the channel and L_{ch} the channel length. The saturated drain-source current Idss of FETs in Table 1. Ne25139-U71 demonstrates the lowest 1/*f* noise because it has the lowest Idss among the Ne25139 series, all of which have identical channel lengths according to the datasheet. Owing to the larger Idss in 3sk166, it also exhibited a higher 1/*f* noise. However, the channel length value is not provided in its datasheet, although it shares the same footprint as that of the Ne25139 series. Compared to using cascode stage with Ne25139 and CF739, employing a single Ne25139 as Q5 results in higher input voltage noise. This is because shortening the two gates of the FET increases the channel length, leading to a reduction in low-frequency noise.

AMP1 was designed for an axial frequency readout and had the highest gain in the relevant frequency range. However, the frequency of the cyclotron is not within this range. Although the cyclotron frequency is usually read out through sideband coupling, which couples the radial motion to the axial motion of the ion, it is also beneficial to directly detect the cyclotron motion using a cryogenic amplifier specifically designed for that frequency range. For this purpose, we developed another cryogenic amplifier, denoted here as AMP2, which is similar to AMP1 but excludes the second common-source amplification stage. The cascode stage comprises two ATF35143 transistors. The measured gain and input voltage noise of AMP2 in the 1–200 MHz frequency range are shown in Fig. 6. At the highest frequency, the amplifier still has a gain of 15 dB. Note that noise peaks in the high-frequency range may originate from the environment.

3.2 Resonator

The other component of the cryogenic detection system can be described as an effective parallel RLC circuit, in experimental realization, manufactured with a solenoidal coil wound on a PTFE core and mounted in a cylindrical housing. The Q value of the tank circuit was strongly influenced by the series resistance and self-capacitance of the coil. Both the ohmic and dielectric losses should be minimized to achieve a high equivalent parallel resistance. Close to the resonance frequency, R_p can be approximated in terms of the capacitor's equivalent series resistance (ESR[1]) and the equivalent winding resistance of the inductor, R_L:

$$R_P \approx \frac{L}{C(ESR + R_L)}. \tag{10}$$

According to this relation, R_p can be increased by minimizing the circuit parameters C, R_L and ESR while maximizing the inductance L. To control these parameters, an inductor is developed as a coil in a shield or housing. The resonator's inductance and capacitance are determined by the size of

[1] The ESR incorporates the capacitor's dielectric and conduction losses. The losses due to electromagnetic radiation of the tuned circuit were neglected.

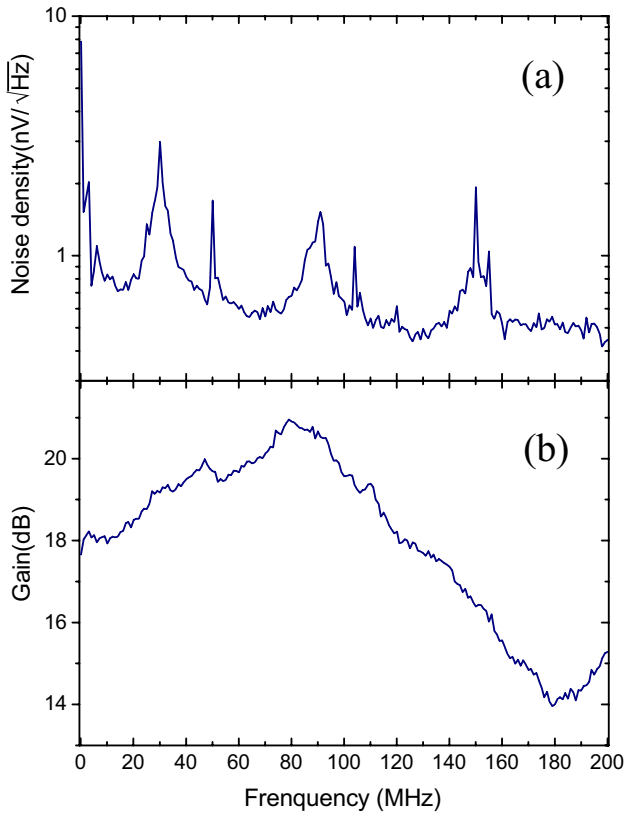

Fig. 6 (Color online) The measured gain (**a**) and input voltage noise density (**b**) of the AMP2 in the frequency range of 1 to 200 MHz

the coil and the shield dimensions. These losses stem mainly from the choice of materials and partly from the geometry. An overview of the materials, geometries, and fabrication processes used in the development of the resonator is provided below.

A resonator wound with superconducting NbTi wires can minimize the conductive loss when operated below the critical temperature of $T_c \approx 9.5$ K, presenting a very low series resistance to the induced current. The conductor of the superconducting wire (manufactured by California Fine Wire) was 75 µm in diameter, and the insulation layer made of PTFE, brought the total diameter of the wire to approximately 100 µm. The thin wire allowed dense winding, enabling the achievement of a large inductance within a limited housing space. Meanwhile, the PTFE insulator, with its low permittivity and low loss tangent, ensured that the dielectric loss remained sufficiently low. The geometry of the resonator is shown in Fig. 7. The body frame of the coil, also made of PTFE, with an outer diameter of 20 mm matching the coil diameter, was divided into 16 chambers. The NbTi wire was wound into three layers within each chamber before crossing the edge of the next chamber. This effectively reduces the self-capacitance. The cylindrical housing, which was approximately 140 mm high and 40 mm wide, including the end caps, was also made of NbTi, and its inner face was polished to mitigate the eddy current effect [45]. In total, the manufactured resonator comprises 900 turns wound across 10 chambers over a total length of 100 mm, yielding a designed inductance of 4.5 mH and a capacitance of 5.6 pF.

Ensuring good heat contact between the wire and PTFE core is crucial because at the phase transition to the superconducting state, electrons condense to the BCS ground state, leading to a decrease in the heat conduction coefficient of NbTi. The windings were fixed to the body frame using PTFE thread-seal tape, and the body was pressed against the bottom plate of the housing using a brass screw. This configuration also ensured mechanical stability of the coil during thermal cycling. Both ends of the coil were soldered to high-conductivity copper wires with 0.7 mm diameters. One end was designed to connect to the trap, namely the "hot end," whereas the other was RF grounded, denoted here as the "cold end." A 1/10 winding tap was present in the coil, where the signal was picked up and fed into the input of the cryogenic amplifier. This design utilized the coil as a self-transformer, effectively reducing the noise from subsequent electronics to the trap.

The measurement setup is illustrated in Fig. 8a. The thermal noise of the resonator was amplified by the cryogenic amplifier mentioned above as well as an RT amplifier before entering the spectrum analyzer. The measured noise spectra are presented in Fig. 8b. To estimate the values rapidly, the Q value of the resonator can be determined from the ratio of the resonance frequency ν_{res} to the width at the -3 dB point below the resonance peak. A more accurate result is obtained by fitting a line-shaped model of the resonator impedance to the experimentally obtained data.

$$Z_{LC}^{-1} = \frac{1}{i\omega L} + i\omega C + \frac{1}{R_p} = \frac{1}{R_p}\left[1 + iQ\left(\frac{\omega}{\omega_{res}} - \frac{\omega_{res}}{\omega}\right)\right]. \tag{11}$$

The resulting resonance frequency ν_{res} is 1.000810 MHz and Q value is 98004(3186). The signal-to-noise ratio, measured as the peak of the resonator to the noise floor, is approximately 25 dB, consistent with our expectations. The spikes occurring at the 50 Hz intervals are likely caused by stray noise from the environment, such as interference from the cold-head supply. Notably, the experimental setup is ultimately cooled with liquid helium instead of the cold head to eliminating such noise.

To determine the inductance and self-capacitance of the coil, we soldered an additional capacitor parallel to it, which shifted the resonance frequency to $\nu_i = \frac{1}{2\pi}\frac{1}{\sqrt{L(C_p+C_i)}}$. By tuning the capacitor C_i to 3 pF, 5 pF and 10 pF, the measured frequencies were shifted to 775.662 kHz, 704.538 kHz and

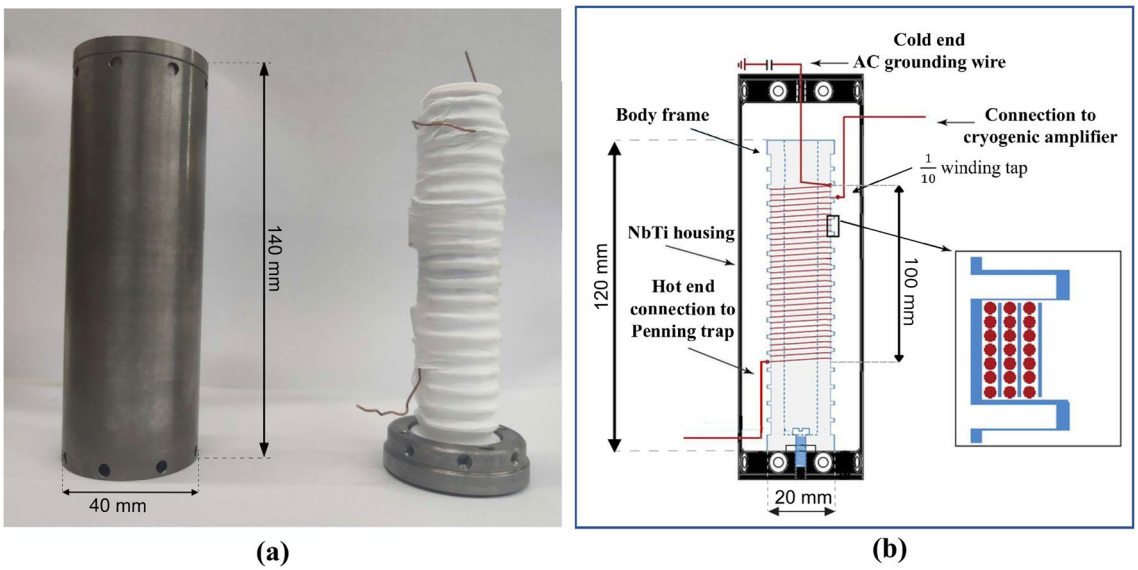

Fig. 7 (Color online) **a** Photograph of the resonator showing a body frame with 900 turns of NbTi wire windings covered by PTFE seal tape, and a housing made of NbTi material. **b** A schematic diagram illustrates the multilayer and multichamber structure of the inner coil windings

593.688 kHz, respectively. Each time the parallel capacitor is changed, it may affect the parasitic capacitance by no more than 1 pF. Consequently, the inductance and self-capacitance of the coil were measured as 5.7 pF and 4.7 mH, respectively, which are consistent with the designed parameters. The Q value is constrained by losses in the coil owing to various factors. The weak solder joint between NbTi and Cu may introduce a fractional series resistance to the coil. Additionally, the superconducting NbTi wire that we utilized features a very thin insulating layer (approximately 10 μm), which could limit the Q value owing to the dielectric losses in the thin insulator. Notably, upon connection to the trap, the quality factor can be significantly influenced by the impedance of the feedthrough and cables, which predominantly determines the final Q value.

4 Summary

A cryogenic electronic system for image charge detection was developed for use in the Shanghai Penning Trap. The system comprises two primary components: a cryogenic amplifier with low noise and high gain and a helical superconducting resonator, which resonantly amplifies the image current of a single ion. This system enables the detection of minute signals from ions, facilitating further amplification and spectral analysis at RT. Low-noise cryogenic amplifiers were engineered in three amplification stages. The initial stage employs a cascode common-source amplifier with two FETs to mitigate the Miller effect. The second stage adopts another common-source design for cascaded amplification, whereas the third stage employs a source follower to ensure impedance matching. The input voltage noise and amplification factors of the amplifiers were measured at the cryogenic stage using various FETs employed at the first transistor position. In the frequency range of 0.1~10 MHz, the highest gain measured was greater than 27 dB for Ne25139-U73, whereas Ne25139-U71 exhibited the lowest 1/f noise. Additionally, we observed a correlation between 1/f noise and the saturated drain-source current in FETs. By shortening the two gates of Ne25139-U71 to increase the channel length, we also achieved a reduction in 1/f noise. To detect the cyclotron motion of the ion directly, we developed another amplifier that can be operated in the frequency range of 1 MHz to 200 MHz, demonstrating an amplification factor exceeding 15 dB at the highest frequency. The helical resonator, which was fabricated with 900 turns of NbTi superconducting wires in three layers, was housed in a cylindrical NbTi enclosure. After the measurements at the cold-head base cryogenic stage, the inductance, self-capacitance, and resonance frequency were determined. The unloaded Q value is 98004. The loss in the coil arises from several factors, including soldering at the NbTi-to-Cu joint and the dielectric loss within the coil. By enhancing the joint contact with a spot welder or high indium solder and ensuring good thermal contact between the wire solder joints and the PTFE core, a lower series resistive loss can be achieved. Additionally, using a thicker insulator for the NbTi wire to increase the spacing between the wires further reduces the dielectric loss, thereby increasing the Q value.

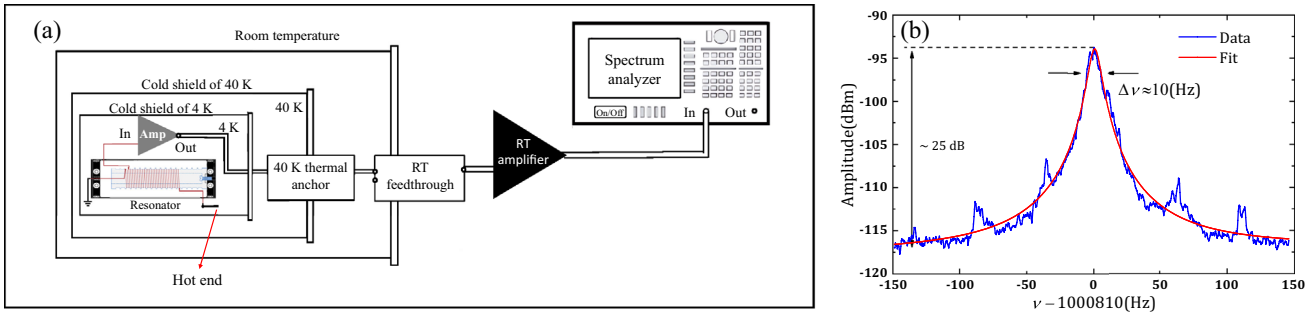

Fig. 8 (Color online) **a** Schematic of the measurement setup for the resonator test at cryogenic stage. The cold end is grounded. The 1/10 winding tap is connected to the cryogenic amplifier (AMP1) for noise signal read out. The signal is amplified by another RT amplifier before undergoing fast Fourier transform analysis by a spectrum analyzer. **b** Resonance spectrum is fitted with parameters ν_{res} = 1.000810 MHz and Q = 98004(3186)

Acknowledgements The authors extend their sincere gratitude to Professors Klaus Blaum and PD. Sven Sturm from the Max Planck Institute for Nuclear Physics for their invaluable discussions on techniques. The authors also thank Dr. Chao Li from Western Superconducting Technologies Co., Ltd. for his kind support with the superconducting materials.

Author contributions All authors contributed to the study conception and design. Material preparation, data collection and analysis were performed by Jia-Rong Wang, Ji-Fei Wu, Tian-Hang Zhang, Jia-Teng Peng, Jia-Lin Liu, Jia-Wei Wang, Yang Shen and Bing-Sheng Tu. The first draft of the manuscript was written by Jia-Rong Wang and all authors commented on previous versions of the manuscript. All authors read and approved the final manuscript.

Data availability The data that support the findings of this study are openly available in Science Data Bank at https://cstr.cn/31253.11.sciencedb.j00186.00756 and https://www.doi.org/10.57760/sciencedb.j00186.00756.

Declarations

Conflict of interest The authors declare that they have no conflict of interest.

References

1. K. Blaum, High-accuracy mass spectrometry with stored ions. Phys. Rep. **425**, 1–78 (2006). https://doi.org/10.1016/j.physrep.2005.10.011
2. T. Yamaguchi, H. Koura, Y.A. Litvinov et al., Masses of exotic nuclei. Prog. Part. Nucl. Phys. **120**, 103882 (2021). https://doi.org/10.1016/j.ppnp.2021.103882
3. W.J. Huang, M. Wang, F.G. Kondev et al., The AME 2020 atomic mass evaluation (I). evaluation of input data, and adjustment procedures*. Chinese Phys. C **45**, 030002 (2021). https://doi.org/10.1088/1674-1137/abddb0
4. M. Wang, W.J. Huang, F.G.K. Kondev et al., The AME 2020 atomic mass evaluation (II). tables, graphs and references*. Chinese Phys. C **45**, 030003 (2021). https://doi.org/10.1088/1674-1137/abddaf
5. J.C. Berengut, D. Budker, C. Delaunay et al., Probing new long-range interactions by isotope shift spectroscopy. Phys. Rev. Lett. **120**, 091801 (2018). https://doi.org/10.1103/PhysRevLett.120.091801
6. K. Ono, Y. Saito, T. Ishiyama et al., Observation of nonlinearity of generalized king plot in the search for New Boson. Phys. Rev. X **12**, 021033 (2022). https://doi.org/10.1103/PhysRevX.12.021033
7. Y.M. Xing, M. Wang, Y.H. Zhang et al., First isochronous mass measurements with two time-of-flight detectors at CSRe. Phys. Scr. **2015**, 014010 (2015). https://doi.org/10.1088/0031-8949/2015/T166/014010
8. M.Z. Sun, X.H. Zhou, M. Wang et al., Precision mass measurements of short-lived nuclides at HIRFL-CSR in Lanzhou. Front. Phys. **13**, 132112 (2018). https://doi.org/10.1007/s11467-018-0844-5
9. X. Zhou, M. Wang, Y.H. Zhang et al., Charge resolution in the isochronous mass spectrometry and the mass of ^{51}Co. Nucl. Sci. Tech. **32**, 37 (2021). https://doi.org/10.1007/s41365-021-00876-0
10. Y.H. Zhang, P. Zhang, X.H. Zhou et al., Isochronous mass measurements of $T_z = -1$ fp-shell nuclei from projectile fragmentation of ^{58}Ni. Phys. Rev. C **98**, 014319 (2018). https://doi.org/10.1103/PhysRevC.98.014319
11. M. Steck, Y.A. Litvinov, Heavy-ion storage rings and their use in precision experiments with highly charged ions. Part. Nucl. Phys. **115**, 103811 (2020). https://doi.org/10.1016/j.ppnp.2020.103811
12. X.L. Tu, X.C. Chen, J.T. Zhang et al., First application of combined isochronous and Schottky mass spectrometry: Half-lives of fully ionized $^{49}Cr^{24+}$ and $^{53}Fe^{26+}$ atoms. Phys. Rev. C **97**, 014321 (2018). https://doi.org/10.1103/PhysRevC.97.014321
13. M. Zach, Mapping the frontiers of the nuclear mass surface. J. Phys. Conf. Ser. **1668**, 012026 (2020). https://doi.org/10.1088/1742-6596/1668/1/012026
14. W.R. Plaß, T. Dickel, C. Scheidenberger, Multiple-reflection time-of-flight mass spectrometry. Int. J. Mass Spectrom. **349**, 134–144 (2013). https://doi.org/10.1016/j.ijms.2013.06.005
15. J. Dilling, K. Blaum, M. Brodeur et al., Penning-trap mass measurements in atomic and nuclear physics. Annu. Rev. Nucl. Part. Sci. **68**, 45–74 (2018). https://doi.org/10.1146/annurev-nucl-102711-094939
16. Y.A. Litvinov, H. Geissel, T. Radon et al., Mass measurement of cooled neutron-deficient bismuth projectile fragments with

time-resolved Schottky mass spectrometry at the FRS-ESR facility. Nucl. Phys. A **756**, 3–38 (2005). https://doi.org/10.1016/j.nuclphysa.2005.03.015
17. X. Xu, J.H. Liu, C.X. Yuan et al., Masses of ground and isomeric states of ^{101}In and configuration-dependent shell evolution in odd-A indium isotopes. Phys. Rev. C **100**, 051303 (2019). https://doi.org/10.1103/PhysRevC.100.051303
18. X.L. Yan, R.J. Chen, M. Wang et al., Characterization of a double Time-Of-Flight detector system for accurate velocity measurement in a storage ring using laser beams. Nucl. Instrum. Methods Phys. Res. Sect. A **931**, 52–59 (2019). https://doi.org/10.1016/j.nima.2019.03.058
19. H.F. Li, S. Naimi, T.M. Sprouse et al., First Application of Mass Measurements with the Rare-RI Ring Reveals the Solar *r*-Process Abundance Trend at $A = 122$ and $A = 123$. Phys. Rev. Lett. **128**, 152701 (2022). https://doi.org/10.1103/PhysRevLett.128.152701
20. S. Naimi, H.F. Li, Y. Abe et al., First application of mass measurements with the rare-RI ring reveals the solar *r*-process abundance trend at $A = 122$ and $A = 123$. J. Phys: Conf. Ser. **1643**, 012058 (2020). https://doi.org/10.1088/1742-6596/1643/1/012058
21. M. Wang, H.S. Xu, Y.H. Zhang et al., Mass Measurement of Short-lived Nuclei at HIRFL-CSR. EPJ Web Conf. **66**, 02107 (2014). https://doi.org/10.1051/epjconf/20146602107
22. C.Y. Fu, Y.H. Zhang, M. Wang et al., Mass measurements for the $T_z = -2$ *fp*-shell nuclei ^{40}Ti, ^{44}Cr, ^{46}Mn, ^{48}Fe, ^{50}Co, and ^{52}Ni. Phys. Rev. C **102**, 054311 (2020). https://doi.org/10.1103/PhysRevC.102.054311
23. Y.M. Xing, C.X. Yuan, M. Wang et al., Isochronous mass measurements of neutron-deficient nuclei from ^{112}Sn projectile fragmentation. Phys. Rev. C **107**, 014304 (2023). https://doi.org/10.1103/PhysRevC.107.014304
24. M. Wang, Y.H. Zhang, X. Zhou et al., Mass measurement of upper *fp*-Shell $N = Z - 2$ and $N = Z - 1$ Nuclei and the importance of three-nucleon force along the $N = Z$ Line. Phys. Rev. Lett. **130**, 192501 (2023). https://doi.org/10.1103/PhysRevLett.130.192501
25. X. Zhou, M. Wang, Y.H. Zhang et al., Mass measurements show slowdown of rapid proton capture process at waiting-point nucleus ^{64}Ge. Nat. Phys. **19**, 1091–1097 (2023). https://doi.org/10.1038/s41567-023-02034-2
26. Y.M. Xing, K.A. Li, Y.H. Zhang et al., Mass measurements of neutron-deficient Y, Zr, and Nb isotopes and their impact on *rp* and *vp* nucleosynthesis processes. Phys. Lett. B **781**, 358–363 (2018). https://doi.org/10.1016/j.physletb.2018.04.009
27. T. Dickel, W.R. Plaß, A. Becker et al., A high-performance multiple-reflection time-of-flight mass spectrometer and isobar separator for the research with exotic nuclei. Nucl. Instrum. Methods Phys. Res. Sect. A **777**, 172–188 (2015). https://doi.org/10.1016/j.nima.2014.12.094
28. P. Schury, M. Wada, Y. Ito et al., First online multireflection time-of-flight mass measurements of isobar chains produced by fusion-evaporation reactions: Toward identification of superheavy elements via mass spectroscopy. Phys. Rev. C **95**, 011305 (2017). https://doi.org/10.1103/PhysRevC.95.011305
29. S.F. Paul, J. Bergmann, J.D. Cardona et al., Mass measurements of $^{60-63}$Ga reduce x-ray burst model uncertainties and extend the evaluated $T =$ lisobaric multiplet mass equation. Phys. Rev. C **104**, 065803 (2021). https://doi.org/10.1103/PhysRevC.104.065803
30. S. Eliseev, K. Blaum, M. Block et al., Phase-imaging ion-cyclotron-resonance measurements for short-lived nuclides. Phys. Rev. Lett. **110**, 082501 (2013). https://doi.org/10.1103/PhysRevLett.110.082501
31. O. Kaleja, B. AnĐelić, O. Bezrodnova et al., Direct high-precision mass spectrometry of superheavy elements with SHIPTRAP. Phys. Rev. C **106**, 054325 (2022). https://doi.org/10.1103/PhysRevC.106.054325
32. D.A. Nesterenko, T. Eronen, A. Kankainen et al., Phase-imaging ion-cyclotron-resonance technique at the JYFLTRAP double Penning trap mass spectrometer. Eur. Phys. J. A **54**, 154 (2018). https://doi.org/10.1140/epja/i2018-12589-y
33. E.M. Lykiardopoulou, C. Izzo, E. Leistenschneider et al., Towards high precision mass measurements of Highly Charged Ions using the Phase-Imaging Ion-Cyclotron-Resonance technique at TITAN. Hyperfine Interact. **241**, 37 (2020). https://doi.org/10.1007/s10751-020-1705-5
34. S. Sturm, F. Köhler, J. Zatorski et al., High-precision measurement of the atomic mass of the electron. Nature **506**, 467–470 (2014). https://doi.org/10.1038/nature13026
35. F. Heiße, F. Köhler-Langes, S. Rau et al., High-precision measurement of the proton's atomic mass. Phys. Rev. Lett. **113**, 033001 (2017). https://doi.org/10.1103/PhysRevLett.119.033001
36. M.J. Borchert, J.A. Devlin, S.R. Erlewein et al., A 16-parts-per-trillion measurement of the antiproton-to-proton charge–mass ratio. Nature **601**, 53–57 (2022). https://doi.org/10.1038/s41586-021-04203-w
37. S.R. Jefferts, T. Heavner, P. Hayes et al., Superconducting resonator and a cryogenic GaAs field-effect transistor amplifier as a single-ion detection system. Rev. Sci. Instrum. **64**, 737–740 (1993). https://doi.org/10.1063/1.1144153
38. S. Ulmer, H. Kracke, K. Blaum et al., The quality factor of a superconducting rf resonator in a magnetic field. Rev. Sci. Instrum. **80**, 12 (2009). https://doi.org/10.1063/1.3271537
39. H. Nagahama, G. Schneider, A. Mooser et al., Highly sensitive superconducting circuits at 700 kHz with tunable quality factors for image-current detection of single trapped antiprotons. Rev. Sci. Instrum. **87**, 11 (2016). https://doi.org/10.1063/1.4967493
40. S. Sturm, I. Arapoglou, A. Egl et al., The ALPHATRAP experiment. Eur. Phys. J. Spec. Top. **227**, 1425–1491 (2019). https://doi.org/10.1140/epjst/e2018-800225-2
41. B. Tu, R. Si, S. Yang et al., Experimental access to observing decay from extremely long-lived metastable electronic states via Penning trap spectrometry. Phys. Rev. Res. **5**, 043014 (2023). https://doi.org/10.1103/PhysRevResearch.5.043014
42. M. Vogel, Particle Confinement in Penning Traps. (Springer Series on Atomic, Optical, and Plasma Physics, vol. 100, Springer International Publishing, Cham, 2018), pp. 45–56 https://doi.org/10.1007/978-3-319-76264-7
43. L.S. Brown, G. Gabrielse, Geonium theory: physics of a single electron or ion in a Penning trap. Rev. Mod. Phys. **58**, 233 (1986). https://doi.org/10.1103/RevModPhys.58.233
44. L.S. Brown, G. Gabrielse, Precision spectroscopy of a charged particle in an imperfect Penning trap. Phys. Rev. A **25**, 2423 (1982). https://doi.org/10.1103/PhysRevA.25.2423
45. L.H. Dixon, in Eddy current losses in transformer windings and circuit wiring. 1988.p. R2–1, SEM600 Unitrode Seminar, (1988)